Nanoscale Res Lett (2009) 4:646–654
DOI 10.1007/s11671-009-9294-x

NANO EXPRESS

Structure and Photoluminescent Properties of ZnO Encapsulated in Mesoporous Silica SBA-15 Fabricated by Two-Solvent Strategy

Qingshan Lu · Zhongying Wang · Jiangong Li · Peiyu Wang · Xialei Ye

Received: 8 January 2009 / Accepted: 5 March 2009 / Published online: 21 March 2009

Abstract The two-solvent method was employed to prepare ZnO encapsulated in mesoporous silica (ZnO/SBA-15). The prepared ZnO/SBA-15 samples have been studied by X-ray diffraction, transmission electron microscope, X-ray photoelectron spectroscopy, nitrogen adsorption–desorption isotherm, and photoluminescence spectroscopy. The ZnO/SBA-15 nanocomposite has the ordered hexagonal mesostructure of SBA-15. ZnO clusters of a high loading are distributed in the channels of SBA-15. Photoluminescence spectra show the UV emission band around 368 nm, the violet emission around 420 nm, and the blue emission around 457 nm. The UV emission is attributed to band-edge emission of ZnO. The violet emission results from the oxygen vacancies on the ZnO–SiO_2 interface traps. The blue emission is from the oxygen vacancies or interstitial zinc ions of ZnO. The UV emission and blue emission show a blue-shift phenomenon due to quantum-confinement-induced energy gap enhancement of ZnO clusters. The ZnO clusters encapsulated in SBA-15 can be used as light-emitting diodes and ultraviolet nanolasers.

Keywords ZnO · Clusters · Mesoporous silica · Photoluminescence

Q. Lu · Z. Wang · J. Li (✉) · P. Wang · X. Ye
Institute of Materials Science and Engineering, Lanzhou University, Lanzhou 730000, China
e-mail: lijg@lzu.edu.cn

Introduction

Semiconductors usually exhibit quantum size effects and electric and optical properties different from bulk materials, when their particle size decreases to nanometer scale [1]. The fabrication strategy for semiconductor nanostructure includes a wide variety of vapor, liquid, and solid state processing routes [2]. Different techniques such as pulsed laser deposition, sputtering, thermal evaporation and condensation, solid state reaction, and chemical method have been employed to fabricate such nanostructures. Among these techniques, the template-assisted synthesis, which involves confined growth of nanostructures because of volume space effect, provides a simple, low-cost, and high-yield synthetic route for a large variety of materials. Among various hard templates such as track-etched polycarbonate, polystyrene sphere (PS) colloidal monolayer template, single-walled carbon nanotube, and anodized aluminum oxide (AAO), ordered mesoporous silica SBA-15 [3] is one prominent example and was used to construct nanostructures because of its uniform pore size, hexagonal array of one-dimensional cylindrical channels, large surface areas, and high thermal stability. Therefore, it is convenient to stabilize highly dispersed ultrafine metal or oxide nanocrystals, nanowires, quantum dots, and clusters in the channels of SBA-15.

ZnO is a multifunctional semiconductor material. Due to the features such as a wide band gap of 3.37 eV, a high exciton binding energy of 60 meV at room temperature, and special electrical and optoelectronic properties [4], a wide range of potential applications [5] from fine photoelectronics, transparent conductive films, solar cell windows, and acoustic wave devices to gas sensing devices excite intensive studies on ZnO nanostructures. In addition to conventional nanoparticles, the various ZnO nanostructures

including quantum dots [6], nanowires [7], nanorods [8], and nanocastles [9] have been found to show unique optical, optoelectronic, and photocatalytic properties. The composite of carbon nanoparticles embedded in ZnO matrix was studied as a solar thermal absorber in solar energy applications [10]. Furthermore, ZnO is a promising material for potential optical applications [11] and has potential application as a short-wave-length light emitting material. Now, a lot of studies are concentrated on tuning the band gap of ZnO by changing the diameter of particle size because of strong size-dependent band gap. All these have excited researches to develop new synthetic methodologies to prepare well-controlled ZnO nanostructures.

Up-to-date, several strategies have been developed to incorporate ZnO in the channels of mesoporous silica SBA-15 and MCM-41 and the pores of zeolites. Two examples are conventional wetness impregnation [12–15] and the improved method with modification of the surface walls followed by loading precursor through affinity interaction [16, 17]. Generally, the former method seems difficult to completely avoid adsorptions of the ZnO precursor on the outer surface of the host template. The uncontrolled ZnO aggregation on the external surface of mesoporous silica will form in subsequent calcinations. The latter method involves complicated process and has low yield. So, it is necessary to develop a simple and low cost novel strategy to prepare ZnO encapsulated in SBA-15 with high quantum size effect and thermal stability.

Recently, a novel strategy called two-solvent method containing hydrophilic and hydrophobic solvents has been applied to prepare $CoFe_2O_4$ nanowires in carbon nanotubes [18, 19]. This method is based on a volume of precursor aqueous solution equal to the pore volume of host template materials which has the advantages of confining and distributing guest species within the pores of host template. Therefore, mesoporous silica SBA-15 could be regarded as a nanoreactor for constructing guest nanomaterials with controlled size and size distribution. The two-solvent method may be employed to prepare a nanocomposite of ZnO clusters supported in mesoporous silica. However, the synthesis of zinc oxide encapsulated in mesoporous silica SBA-15 by the two-solvent method has not been studied so far.

In our present work, we prepared a nanocomposite of ZnO clusters supported in mesoporous silica (or ZnO/SBA-15) via the two-solvent synthetic route. The structure and photoluminescent properties of the ZnO/SBA-15 nanocomposite were studied. The results show that ZnO clusters are distributed in the channels of SBA-15 without aggregations found on the external surface of SBA-15. The UV and blue emissions show a significant blue shift due to quantum size effect compared to the emission of the bulk counterpart reported in the literatures.

Experimental Section

Preparation

The ZnO/SBA-15 nanocomposite was prepared by incorporating zinc nitrate precursor into the channels of mesoporous silica SBA-15 and subsequent calcination. Parent mesoporous silica SBA-15 was synthesized according to the reported process [20]. A typical synthetic procedure was carried out as follows: 4 g of triblock copolymer P123 $[HO(CH_2CH_2O)_{20}(CH_2CH(CH_3)O)_{70}(CH_2CH_2O)_{20}H$, abbreviated as $EO_{20}PO_{70}EO_{20}]$, was mixed with 120 mL of 2 M hydrochloric acid (HCl) and 30 mL of deionized water. The mixture was stirred at 38 °C until P123 was completely dissolved. A total of 8.5 g of tetraethyl orthosilicate (TEOS) was added to this solution under vigorous stirring. The final mixture was stirred at 38 °C for 24 h, then transferred into a teflon-lined autoclave, and kept in the autoclave at 100 °C for 24 h under static condition for hydrothermal treatment. Finally, the formed white precipitates were filtered, washed with water, and dried at room temperature. The extracted mesoporous silica SBA-15 was obtained by removing P123 with ethanol extraction method under refluxing condition.

The procedure of incorporating ZnO into the channels of SBA-15 is as follows [21]. A total of 1 g of extracted mesoporous silica SBA-15 was suspended in 20 mL of *n*-hexane as the first hydrophobic solvent; and the mixture was stirred for 2 h. A total of 0.98 mL of zinc nitrate solution of different concentrations as the second hydrophilic solvent was added to the above mixture dropwise. The resulting solution was vigorously stirred until a paste-like product was obtained. The paste-like product was dried for 12 h in air at room temperature. Finally, ZnO/SBA-15 nanocomposite was obtained by calcining the dried (paste-like) product at 500 °C for 4 h at a heating rate of 1 °C/min in air. The ZnO/SBA-15 nanocomposites with different ZnO loadings are referred as x wt% ZnO/SBA-15, where x represents the weight percentage of ZnO in the nanocomposite.

Characterizations

Low-angle and wide-angle X-ray diffraction (XRD) measurements were carried out on a Rigaku D/Max-2400 X-ray diffractometer using CuK_α radiation in $\theta - 2\theta$ scan mode. High resolution transmission electron microscope (HRTEM) observations and energy dispersive spectroscopy (EDS) measurements were conducted on a JEOL JEM 2010 electron microscope operated at 200 kV. X-ray photoelectron spectroscopy (XPS) measurements were carried out on a PHI-5702 spectrometer (Physical Electronics, Inc.) using an AlK_α X-ray source (1486.7 eV). The energy scale was

internally calibrated by referencing to the binding energy of the C 1s peak of a carbon contaminant at 284.6 eV. Nitrogen adsorption–desorption isotherms were measured by a Micromeritics ASAP2010 system. Barrett–Emmett–Tellter (BET) method in the relative pressure P/P_0 range of 0.01–0.20 was applied for calculating specific surface areas. The pore volume was determined from the adsorption branch of the N_2 isotherm curve at the $P/P_0 = 0.97$ signal point. The pore diameter was derived from the maximum of the pore size distribution curve obtained using Barrett–Joyner–Halenda (BJH) method based on the adsorption branch of the N_2 isotherm curve. Room temperature photoluminescence (PL) spectra were recorded on a FLS-920T fluorescence spectrophotometer with Xe 900 (450 W xenon arc lamp) as the light source using an excitation wavelength of 325 nm.

Results and Discussion

The schematic drawing for the structure formation mechanism of the ZnO/SBA-15 nanocomposite is shown in Fig. 1. This synthetic approach is based on the absorption of hydrophilic zinc nitrate solution into hydrophilic channels of SBA-15 by capillary forces due to the interaction between the polar solvent and the hydrophilic part of the channels. ZnO forms inside the channels of SBA-15 during calcination.

Figure 2 shows the low-angle XRD patterns of the extracted mesoporous silica SBA-15 and the ZnO/SBA-15 nanocomposite. The low-angle XRD pattern of the extracted SBA-15 exhibits three well-resolved diffraction peaks at $2\theta = 0.84°$, 1.45°, and 1.68°, and the corresponding d spacings are 10.5, 6.0, and 5.3 nm, respectively. The d spacing ratios of three peaks are exactly $1:1/\sqrt{3}:1/2$; these three diffraction peaks can be indexed as (100), (110), and (200) diffractions associated with highly ordered mesoporous silica SBA-15 with a two-dimensional hexagonal symmetry (space group p6mm) [20]. In comparison to the extracted SBA-15, the ZnO/SBA-15 nanocomposites show low angle XRD patterns similar to that of SBA-15. Obviously, the hexagonal ordered structures are retained well even after the mixing and calcination process, indicating that the introduction of ZnO into SBA-15 does not collapse the mesoscopic order of a two-dimensional hexagonal structure. It is confirmed that SBA-15 has a thermal stability when used as hard template. The main diffraction peaks of the extracted SBA-15, 8 wt% ZnO/SBA-15, 15 wt% ZnO/SBA-15, and 20 wt% ZnO/SBA-15 with $2\theta = 0.84°$, 0.89°, 0.88° and 0.86° are shown in Fig. 2, respectively. It is obvious that all low-angle XRD peaks of the ZnO/SBA-15 nanocomposite shift to high angles, when compared to the extracted SBA-15. This is due to the contraction of the silica frameworks during calcination. In addition, the d_{100} interplanar spacings of 8 wt% ZnO/SBA-15, 15 wt% ZnO/SBA-15, and 20 wt% ZnO/SBA-15 are 9.9, 10.0, and 10.3 nm, respectively. A clear increase of the d_{100} interplanar spacing has been observed with increasing ZnO loading. This suggests that the mesoporous structure of the ZnO/SBA-15 nanocomposite expands with increasing ZnO loading [16, 22]. Based on $a_0 = 2d_{100}/\sqrt{3}$ [20], where a_0 represents the pore-to-pore distance of the hexagonal structure, the unit cell parameter a_0 of the ZnO/SBA-15 nanocomposite is calculated to be 11.4, 11.6, and 11.9 nm for the ZnO loadings of 8 wt%, 15 wt%, and 20 wt%, respectively.

Figure 3 shows wide-angle XRD patterns of the ZnO/SBA-15 nanocomposites with different ZnO loadings. All the ZnO/SBA-15 nanocomposites exhibit the broad diffuse peaks attributed to the non-crystalline silica and ZnO. No diffraction peaks of the ZnO crystalline phase were detected in the wide-angle XRD patterns, even for the high weight percentage of 20 wt% ZnO, indicating that ZnO in the ZnO/SBA-15 nanocomposites is non-crystalline or may exist as clusters with ultrafine particle sizes. This result is same as that reported for other metal oxides clusters inside the channels of SBA-15 [12, 23].

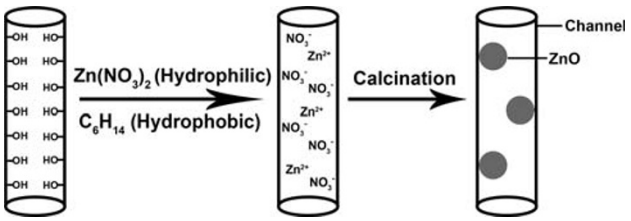

Fig. 1 Schematic drawing for the structure formation mechanism of ZnO/SBA-15 nanocomposite

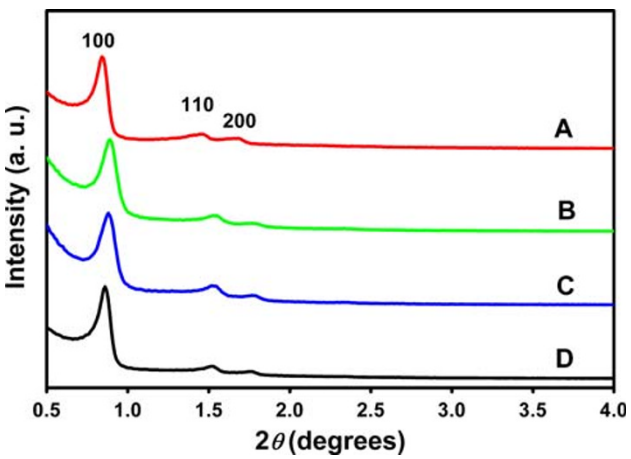

Fig. 2 Low-angle XRD patterns of the extracted SBA-15 (curve A), the 8 wt% ZnO/SBA-15 nanocomposite (curve B), the 15 wt% ZnO/SBA-15 nanocomposite (curve C), and the 20 wt% ZnO/SBA-15 nanocomposite (curve D)

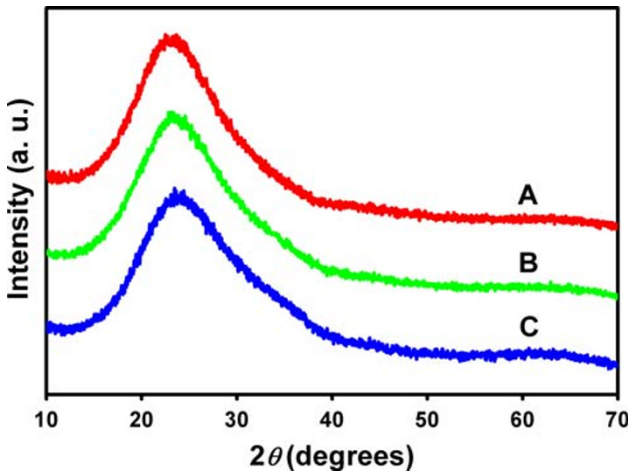

Fig. 3 Wide-angle XRD patterns of the ZnO/SBA-15 nanocomposites with ZnO loadings of 8 wt% (curve A), 15 wt% (curve B), and 20 wt% (curve C)

In order to obtain more information about the existence and form of ZnO in the ZnO/SBA-15 nanocomposites, the 20 wt% ZnO/SBA-15 nanocomposite was calcined at different temperatures and analyzed by XRD. As shown in Fig. 4, the 20 wt% ZnO/SBA-15 nanocomposite calcined at 500 °C yields only a broad diffuse peak which should be attributed to non-crystalline silica and ZnO. The 20 wt% ZnO/SBA-15 nanocomposite calcined at 650 °C yields the seven diffraction peaks overlapped on the diffuse peak of the non-crystalline silica. The seven diffraction peaks at $2\theta = 31.74°$, 34.36°, 36.28°, 47.64°, 56.58°, 62.90°, and 67.90° can be indexed as (100), (002), (101), (102), (110), (103), and (112) diffractions of the ZnO wurtzite [6], respectively. Therefore, ZnO in the 20 wt% ZnO/SBA-15 nanocomposite calcined at 650 °C exists in form of the crystalline ZnO wurtzite phase. ZnO in the 20 wt%

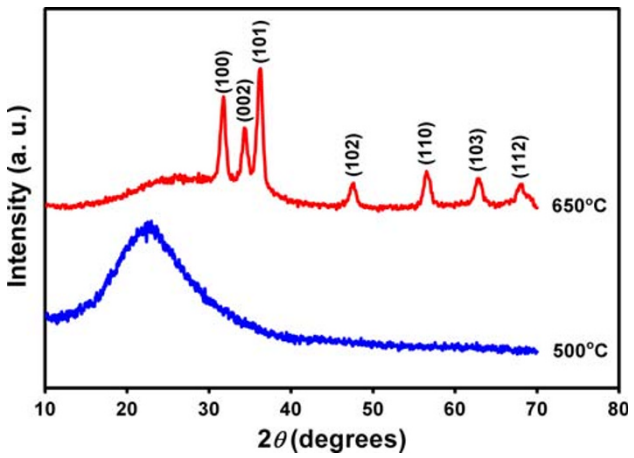

Fig. 4 Wide-angle XRD patterns of the 20 wt% ZnO/SBA-15 nanocomposite calcined at different temperatures

ZnO/SBA-15 nanocomposite calcined at 500 °C exists in form of the non-crystalline ZnO phase or ZnO clusters. Vepřek [24] reported that nanocrystalline Si with the average crystallite size less than 3.5 nm can reduce its excess energy stored in the high density grain boundaries, if it transforms structurally from a nanocrystalline into a non-crystalline structure. That is to say, Si can exist stably in the form of non-crystalline phase when the clusters are smaller than 3.5 nm and in the form of crystalline phase when the crystallites are larger than 3.5 nm. In our study, the precursor aqueous solution is homogeneous distributed on the large inner surface areas of SBA-15. In subsequent calcination at 500 °C, the $Zn(NO_3)_2$ decomposes and the ultrafine ZnO clusters may form. When the formed ZnO clusters are too fine, the ZnO clusters may exist stably in the form of non-crystalline phase. With the annealing temperature increasing to 650 °C, the average size of the ZnO clusters will increase to reach the critical size of the crystalline phase. Then ZnO exists stably in the form of the crystalline structure with a low energy state. Li et al. [25] reported the thermal decomposition of $Zn(NO_3)_2$ to ZnO at the calcination temperature of 150 °C. The ZnO clusters formed in the channels of SBA-15 are so fine that they exist in amorphous state [16]. The ZnO clusters can exist stably at a higher temperature (500 °C) (Fig. 4), which enlarges the scope of applications.

The mesoporous structures of the ZnO/SBA-15 nanocomposite were studied by the TEM observations. Figure 5 shows the TEM micrographs of the 15 wt% ZnO/SBA-15 nanocomposite. The low magnification TEM micrograph in Fig. 5a shows the overall morphology of the ZnO/SBA-15 nanocomposite. The parallel straight channels (Fig. 5b) can be observed with the incident electron beam perpendicular to the channels. When observed with the incident beam parallel to the channels, as shown in Fig. 5c, the 15 wt% ZnO/SBA-15 nanocomposite shows the highly ordered honeycomb-like pore array structure. The diameter of the uniform pores is about 5.9 nm. The ZnO/SBA-15 nanocomposite has a two-dimensional hexagonal mesoporous structure same as SBA-15. The unit cell parameter a_0 (the distance between two neighboring pore centers) is about 11.6 nm, which is in good agreement with 11.6 nm determined by the XRD analysis. The ZnO clusters could not be observed in the channels through TEM investigations (Fig. 5b). This may be due to the fact that the image contrast between the silica framework and ZnO clusters is weak, as in the case of ZnO clusters encapsulated inside the micropores of zeolite [14].

The EDS analysis was carried out on the 15 wt% ZnO/SBA-15 nanocomposite with the EDS attachment on the TEM. Figure 6 illustrates the EDS pattern of the 15 wt% ZnO/SBA-15 nanocomposite. The C and Cu elements come from the supporting carbon film and the copper grid,

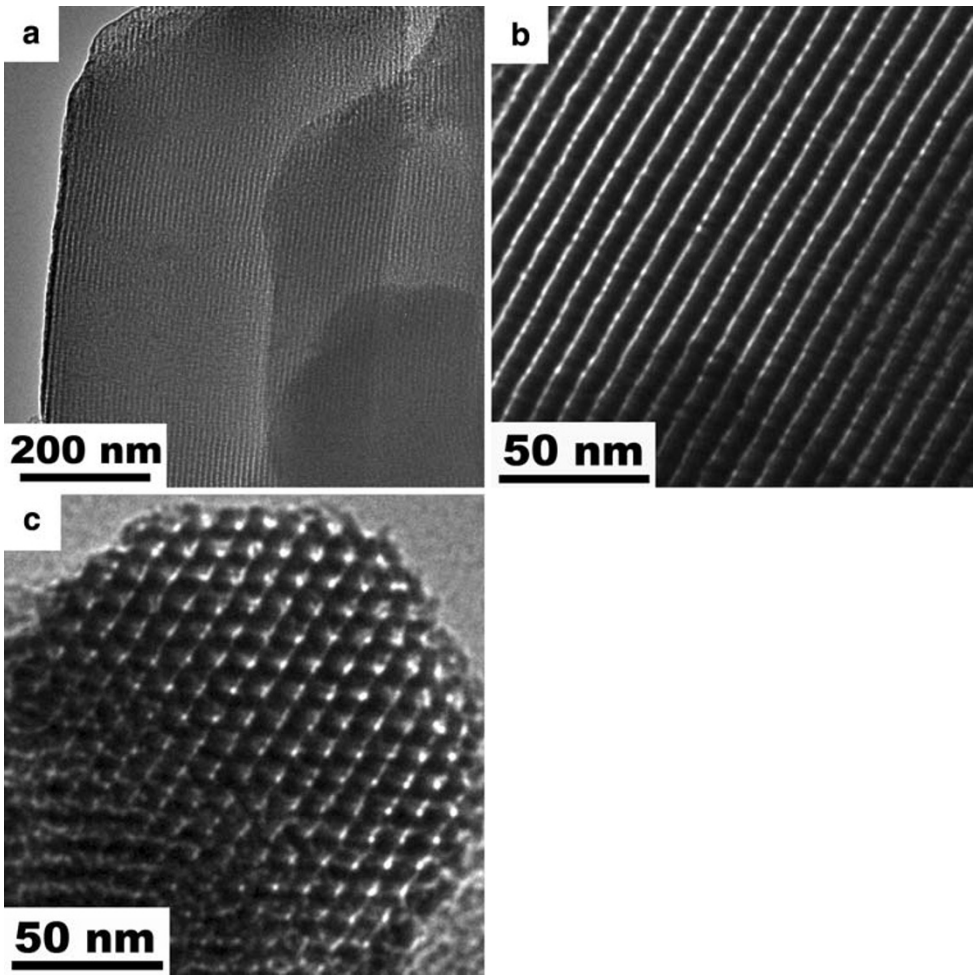

Fig. 5 Low magnification TEM micrograph of the 15 wt% ZnO/SBA-15 nanocomposite (**a**) and high magnification TEM micrographs observed with the electron beam perpendicular to the channels (**b**) and parallel to the channels (**c**)

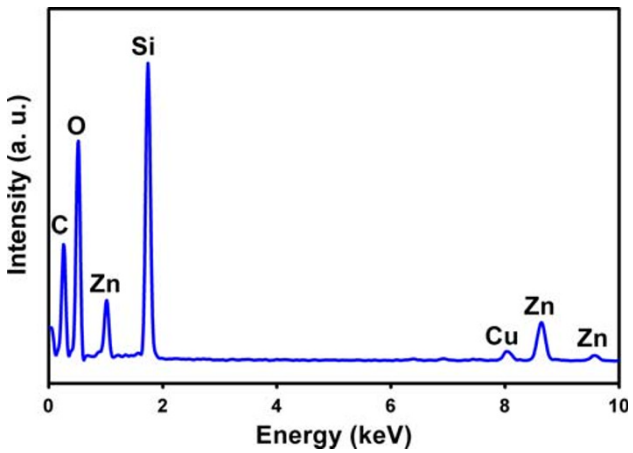

Fig. 6 EDS pattern of the 15 wt% ZnO/SBA-15 nanocomposite

respectively. The strong zinc signals can be clearly detected, confirming the presence of Zn element in ZnO/SBA-15 nanocomposite.

To obtain the additional evidence for confirming the presence of ZnO in the ZnO/SBA-15 nanocomposite, the XPS was employed to determine the chemical state of the zinc element in the ZnO/SBA-15 nanocomposite. Figure 7 depicts the typical XPS spectra of the ZnO/SBA-15 nanocomposite. The peaks around 102.9 eV, 532.2 eV and 1021.9 eV were detected. The peak at a binding energy of 102.9 eV is from Si 2p which can be assigned to silica in SBA-15 [26]. The O 1s peak centered at about 532.2 eV is asymmetric, indicating the presence of more than one chemical environment for oxygen species. The O 1s peak can be fitted with two Gaussian peaks. The weaker shoulder peak at about 530.1 eV can be attributed to the oxygen in pure ZnO [27]. The main peak at about 532.2 eV can be assigned to the oxygen in the non-crystalline silica of SBA-15. In our work, most of oxygens detected by XPS are from non-crystalline silica walls of SBA-15. It is well-known that the valence electron density of O in the Si–O–Si bond is lower than that in the Zn–O–Zn bond, due to the higher electronegativity of Si (1.9) than that of Zn (1.65) [28]. A peak at 1021.9 eV (Fig. 7c) is ascribed to the core level of Zn $2p_{3/2}$ of ZnO [29]. The XPS results confirm that ZnO exists in the ZnO/SBA-15 nanocomposite.

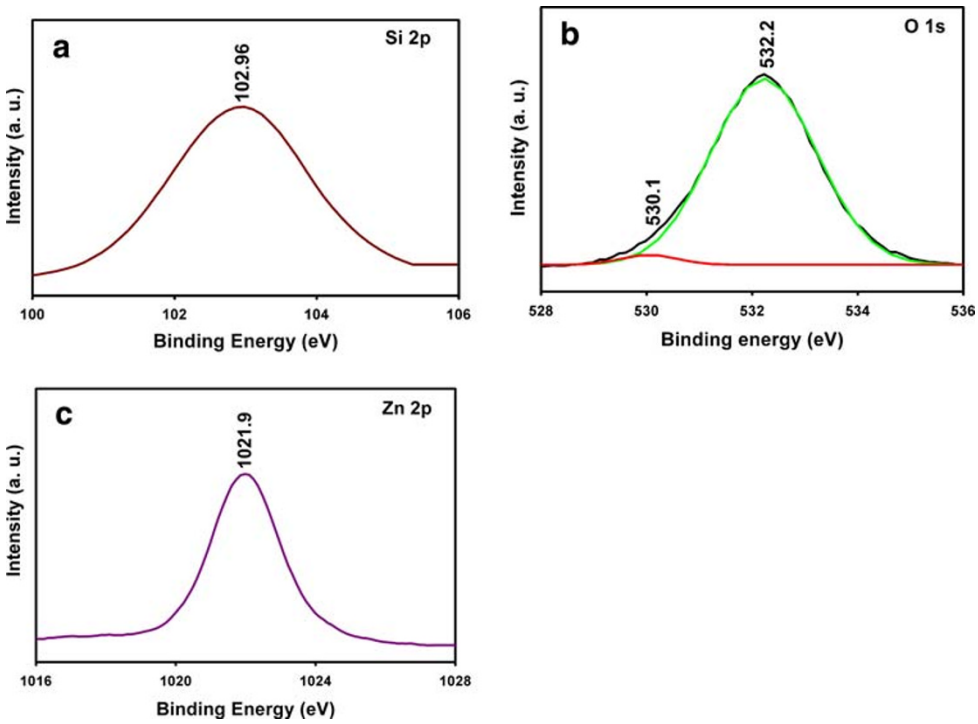

Fig. 7 XPS spectra of the 15 wt% ZnO/SBA-15 nanocomposite: **a** Si 2p, **b** O 1s, and **c** Zn 2p

Figure 8 shows the nitrogen adsorption–desorption isotherms of the extracted SBA-15 and the ZnO/SBA-15 nanocomposites with different ZnO loadings. All the samples show the type IV isotherms with H1-type hysteresis loops defined by IUPAC, typical for mesoporous materials with two-dimensional hexagonal structures [30]. There is no change in the isotherm type observed, proving that well ordered mesoporous cylinder channels are well conserved during the formation of ZnO clusters inside SBA-15, which is coincident with the results obtained from the low-angle XRD and TEM analysis. Physicochemical parameters of the samples are summarized in Table 1. The BET surface area, pore diameter, and pore volume of the ZnO/SBA-15 nanocomposite decrease with increasing ZnO loading. This implies that ZnO should exist in the channels of SBA-15. In addition, the inflection point of the capillary condensation step on the isotherm shifts to lower relative pressure with increasing ZnO loading, indicating the reduction of the mesopore size. This also suggests that ZnO should be successfully incorporated into the channels of SBA-15. In our work, the extracted SBA-15 has a high density of silanol groups on the channel wall surface, and the surface is hydrophilic [31]. During the impregnation process, it is thought to be beneficial for the homogeneous incorporation of high loading of hydrophilic zinc nitrate solution into SBA-15 due to capillary forces. So, the two-solvent strategy provides an elegant route for loading various substances into porous and hollow structure.

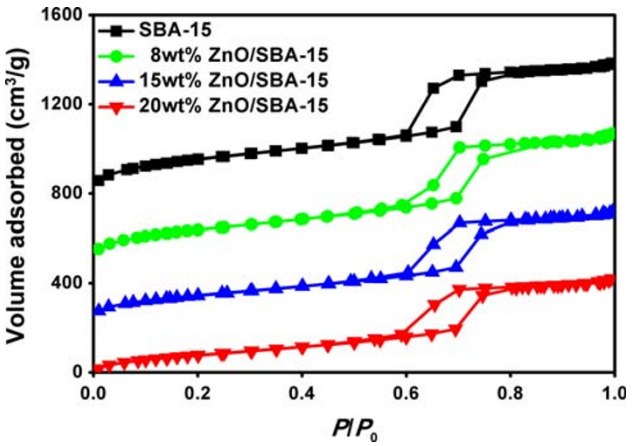

Fig. 8 Nitrogen physisorption isotherms of the extracted SBA-15 and the ZnO/SBA-15 nanocomposites with different ZnO loadings. For a better view, the data of Y axis for the extracted SBA-15, the 8 wt% ZnO/SBA-15, the 15 wt% ZnO/SBA-15, and the 20 wt% ZnO/SBA-15 nanocomposite were shifted by 730, 450, 190 and −60 units, respectively

Combining the above low-angle XRD and TEM analysis results, the ZnO/SBA-15 nanocomposites have the ordered hexagonal mesostructures of SBA-15. The EDS analysis shows the presence of the Zn element in the ZnO/SBA-15 nanocomposites. The XPS analysis confirms that ZnO exists in the ZnO/SBA-15 nanocomposite. The wide-angle XRD shows that ZnO in the ZnO/SBA-15 nanocomposite calcined at 500 °C exists in the non-crystalline state. Nitrogen adsorption–desorption isotherms proves that ZnO

Table 1 Physicochemical parameters derived from nitrogen physisorption and XRD datas for different samples (d_{100} is the interplanar spacing of the hexagonal structure; a_0 represents the pore-to-pore distance of the hexagonal structure)

Samples	d_{100} (nm)	a_0 (nm)	S_{BET} (m^2/g)	Pore diameter (nm)	Pore volume (cm^3/g)
Extracted SBA-15	10.5	12.1	807	6.41	0.985
8 wt% ZnO/SBA-15	9.9	11.4	683	6.11	0.921
15 wt% ZnO/SBA-15	10.0	11.6	564	6.07	0.794
20 wt% ZnO/SBA-15	10.3	11.9	498	6.04	0.716

exists in the channels of SBA-15. These observed results suggest that ZnO may exist as non-crystalline clusters in the channels of SBA-15, as the reported intrapore formation of guest species inside mesoporous silica [32, 33].

The photoluminescent properties of the pure mesoporous silica SBA-15 and the ZnO/SBA-15 nanocomposites were characterized by the PL measurements with an excitation wavelength of 325 nm at room temperature. Figure 9 shows the photoluminescence spectra of SBA-15 and the ZnO/SBA-15 nanocomposites with different ZnO loadings. The broad emission band of the pure SBA-15 is centered at about 402 nm, and the luminescence intensity is very weak, in comparison to that of the ZnO/SBA-15 nanocomposites. The ZnO/SBA-15 nanocomposites yield a strong emission band at about 370 nm. With the ZnO loading increasing from 0 to 15 wt%, the intensity of this emission band increases. The 20 wt% ZnO/SBA-15 nanocomposite presents an almost same photoluminescence spectrum as the 15 wt% ZnO/SBA-15 nanocomposite. Therefore, it is reasonable to believe that the emission band around 370 nm arises from the ZnO clusters encapsulated in the channels of SBA-15.

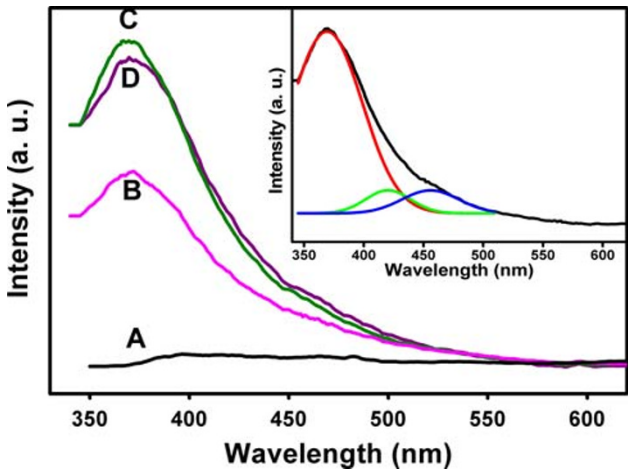

Fig. 9 Photoluminescence spectra of the extracted SBA-15 (curve A), the 8 wt% ZnO/SBA-15 nanocomposite (curve B), the 15 wt% ZnO/SBA-15 nanocomposite (curve C), and the 20 wt% ZnO/SBA-15 nanocomposite (curve D) upon excitation at 325 nm. The inset shows the fitted peaks

It is commonly known that ZnO exhibits the UV near-band-edge emission peak at around 380 nm and the visible emission band ranging from 440 to 600 nm [34]. In general, the emission band in the visible region is associated with structural defects in ZnO [5]. The UV near-band-edge emission peak is attributed to the recombination of free excitons [35] and depends on the ZnO particle size due to quantum size effect.

In our work, the emission band centered at about 370 nm can be fitted by three emission Gaussian peaks shown in the inset in Fig. 9; these three peaks are located at 368 nm, 420 nm, and 457 nm, respectively. Obviously, the UV emission peak centered at 368 nm should be ascribed to the radiative transition in electron-hole recombination process [36]. Usually, ZnO exhibits the UV near-band-edge emission peak at around 380 nm. It is known that the band gap width increases as the particle size decreases, if the size of the ZnO particle decreases to the order of the Bohr radius. The band edge emission shows a blue shift [6]. The blue shift of the UV near-band-edge emission of the ZnO/SBA-15 nanocomposite is observed due to a quantum-confinement-induced energy gap enhancement of the ZnO clusters, and the blue shift to short wavelength is much larger than those reported for mesoporous silica supported ZnO [12, 13, 15, 17]. The UV emission is broad. This may be correlated to defect states of the ZnO clusters, such as the bound exciton and the acceptor–donor pairs. This phenomenon is similar to the case of ZnO quantum dots [28]. The violet luminescence centered at 420 nm is also observed. Recently, Shi et al. [17] reported that the violet luminescence was observed from MCM-41 supported ZnO clusters, which is due to radiative transition between the interface traps and the valence band. The interface traps exist within the depletion regions at the ZnO–SiO_2 boundaries [17]. In our work, the mesoporous silica SBA-15 has a large surface areas about 806 m^2/g determined by N_2 adsorption. The ZnO–SiO_2 interface traps exist in the ZnO/SBA-15 nanocomposites because of the distribution of the ultrafine ZnO clusters in SBA-15. The violet luminescence of the ZnO/SBA-15 nanocomposite centered at 420 nm should be attributed to the radiative transitions between the interface traps and the valence band. Similar results have also been reported in the ZnO/SBA-15

nanocomposite [12]. The weak and broad blue emission band centered at 457 nm is a deep-level emission originated from the oxygen vacancies or interstitial zinc ions of ZnO [12]. The blue shift to short wavelength was also observed, when compared to the value of 480 nm in the SBA-15 supported ZnO [12]. It is found that the blue shift in the visible emission with decreasing particle size closely follows the blue shift in the band edge emission. This phenomenon is similar to the reported results for the ZnO quantum particle thin films [35]. Due to its photoluminescent properties, the ZnO/SBA-15 nanocomposite has the potential applications as ultra-violet light-emitting diodes, laser diodes, and other optical devices. Besides, the ZnO/SBA-15 nanocomposite may be useful for detecting the nitrosamine content in solution, suggesting its potential applications in sensing carcinogens such as *N*′-nitrosonornicotine (NNN) in environment.

Conclusions

The two-solvent method was employed to prepare the nanocomposites of the ZnO clusters supported in SBA-15. The prepared ZnO/SBA-15 nanocomposites with high loadings of ZnO keeps well ordered hexagonal mesoporous structure of SBA-15. ZnO in the ZnO/SBA-15 nanocomposite calcined at 500 °C exists in form of non-crystalline clusters distributed in the channels of SBA-15. Room temperature photoluminescence spectra show three emission bands assigned to the UV band-edge emission (368 nm), the violet emission (420 nm), and the blue emission (457 nm). The blue shift of the UV band-edge emission and the blue emission for the ZnO/SBA-15 nanocomposites indicates that the ZnO clusters supported in SBA-15 have quantum size effect. The ZnO/SBA-15 nanocomposites have potential application as a short-wavelength light emitting material.

Acknowledgments This work was supported by the International S&T Cooperation Program (ISCP) under 2008DFA50340, MOST, China and the National Natural Science Foundation of China under 50872046.

References

1. C. Burda, X. Chen, R. Narayanan, M.A. El-Sayed, Chem. Rev. **105**, 1025 (2005). doi:10.1021/cr030063a
2. S.C. Tjong, H. Chen, Mater. Sci. Eng. R Rep. **45**, 1 (2004). doi:10.1016/j.mser.2004.07.001
3. D. Zhao, Q. Huo, J. Feng, B.F. Chmelka, G.D. Stucky, J. Am. Chem. Soc. **120**, 6024 (1998). doi:10.1021/ja974025i
4. J.W.P. Hsu, D.R. Tallant, R.L. Simpson, N.A. Missert, R.G. Copeland, Appl. Phys. Lett. **88**, 252103 (2006). doi:10.1063/1.2214137
5. Ü. Özgür, Y.I. Alivov, C. Liu, A. Teke, M.A. Reshchikov, S. Doğan, V. Avrutin, S.-J. Cho, H. Morkoç, J. Appl. Phys. **98**, 041301 (2005). doi:10.1063/1.1992666
6. K.F. Lin, H.M. Cheng, H.C. Hsu, L.J. Lin, W.F. Hsieh, Chem. Phys. Lett. **409**, 208 (2005). doi:10.1016/j.cplett.2005.05.027
7. Z.K. Tang, G.K.L. Wong, P. Yu, M. Kawasaki, A. Ohtomo, H. Koinuma, Y. Segawa, Appl. Phys. Lett. **72**, 3270 (1998). doi:10.1063/1.121620
8. L. Xu, Q. Chen, D. Xu, J. Phys. Chem. C **111**, 11560 (2007). doi:10.1021/jp071536a
9. X. Wang, J. Song, Z.L. Wang, Chem. Phys. Lett. **424**, 86 (2006). doi:10.1016/j.cplett.2006.04.013
10. G. Katumba, B.W. Mwakikunga, T.R. Mothibinyane, Nanoscale Res. Lett. **3**, 421 (2008). doi:10.1007/s11671-008-9172-y
11. M. Sanmyo, Y. Tomita, K. Kobayashi, Chem. Mater. **15**, 819 (2003). doi:10.1021/cm025747y
12. Q. Jiang, Z.Y. Wu, Y.M. Wang, Y. Cao, C.F. Zhou, J.H. Zhu, J. Mater. Chem. **16**, 1536 (2006). doi:10.1039/b516061h
13. G.Q. Tang, Y. Xiong, L.Z. Zhang, G.L. Zhang, Chem. Phys. Lett. **395**, 97 (2004). doi:10.1016/j.cplett.2004.07.067
14. J. Chen, Z. Feng, P. Ying, C. Li, J. Phys. Chem. B **108**, 12669 (2004). doi:10.1021/jp048746x
15. W. Zeng, Z. Wang, X.F. Qian, J. Yin, Z.K. Zhu, Mater. Res. Bull. **41**, 1155 (2006). doi:10.1016/j.materresbull.2005.11.003
16. W.H. Zhang, J.L. Shi, L.Z. Wang, D.S. Yan, Chem. Mater. **12**, 1408 (2000). doi:10.1021/cm990740a
17. H.G. Chen, J.L. Shi, H.R. Chen, J.N. Yan, Y.S. Li, Z.L. Hua, Y. Yang, D.S. Yan, Opt. Mater. **25**, 79 (2004). doi:10.1016/S0925-3467(03)00229-5
18. C. Pham-Huu, N. Keller, C. Estournès, G. Ehret, M.J. Ledoux, Chem. Commun. (Camb) **1882** (2002). doi:10.1039/b203787b
19. N. Keller, C. Pham-Huu, T. Shiga, C. Estournès, J.-M. Grenèche, M.J. Ledoux, J. Magn. Magn. Mater. **272–276**, 1642 (2004). doi:10.1016/j.jmmm.2003.12.228
20. D. Zhao, J. Feng, Q. Huo, N. Melosh, G.H. Frederickson, B.F. Chmelka, G.D. Stucky, Science **279**, 548 (1998). doi:10.1126/science.279.5350.548
21. M. Imperor-Clerc, D. Bazin, M.-D. Appay, P. Beaunier, A. Davidson, Chem. Mater. **16**, 1813 (2004). doi:10.1021/cm035353m
22. B.J. Aronson, C.F. Blanford, A. Stein, Chem. Mater. **9**, 2842 (1997). doi:10.1021/cm970180k
23. Y.M. Wang, Z.Y. Wu, L.Y. Shi, J.H. Zhu, Adv. Mater. **17**, 323 (2005). doi:10.1002/adma.200400860
24. S. Vepřek, Z. Iqbal, F.-A. Sarott, Philos. Mag. B **45**, 137 (1982). doi:10.1080/13642818208246392
25. J. Chen, Z. Feng, P. Ying, M. Li, B. Han, C. Li, Phys. Chem. Chem. Phys. **6**, 4473 (2004). doi:10.1039/b407913b
26. J. George, S. Shylesh, A.P. Singh, Appl. Catal. A **290**, 148 (2005). doi:10.1016/j.apcata.2005.05.012
27. L. Fernández, N. Garro, J.E. Haskouri, M. Pérez-Cabero, J. Álvarez-Rodríguez, J. Latorre, C. Guillem, A. Beltrán, D. Beltrán, P. Amorós, Nanotechnology **19**, 225603 (2008). doi:10.1088/0957-4484/19/22/225603
28. Z. Fu, B. Yang, L. Li, W. Dong, C. Jia, W. Wu, J. Phys. Condens. Matter. **15**, 2867 (2003). doi:10.1088/0953-8984/15/17/335
29. S. Gao, H. Zhang, R. Deng, X. Wang, D. Sun, G. Zheng, Appl. Phys. Lett. **89**, 123125 (2006). doi:10.1063/1.2357031
30. M. Kruk, M. Jaroniec, Chem. Mater. **13**, 3169 (2001). doi:10.1021/cm0101069
31. A. Rumplecker, F. Kleitz, E.-L. Salabas, F. Schüth, Chem. Mater. **19**, 485 (2007). doi:10.1021/cm0610635
32. F.J. Brieler, P. Grundmann, M. Froba, L. Chen, P.J. Klar, W. Heimbrodt, H.-A. Krug von Nidda, T. Kurz, A. Loidl, J. Am. Chem. Soc. **126**, 797 (2004). doi:10.1021/ja038960j

33. M. Chatterjee, T. Iwasaki, Y. Onodera, T. Nagase, Catal. Lett. **61**, 199 (1999). doi:10.1023/A:1019097511263
34. S. Cho, J. Ma, Y. Kim, Y. Sun, G.K.L. Wong, J.B. Ketterson, Appl. Phys. Lett. **75**, 2761 (1999). doi:10.1063/1.125141
35. E.M. Wong, P.C. Searson, Appl. Phys. Lett. **74**, 2939 (1999). doi:10.1063/1.123972
36. B. Cao, W. Cai, H. Zeng, G. Duan, J. Appl. Phys. **99**, 073516 (2006). doi:10.1063/1.2188132